gzK-colour-selected star-forming galaxies in the *AKARI* NEP-Deep Field

Monthly Notices of the ROYAL ASTRONOMICAL SOCIETY

MNRAS **502,** 1933–1946 (2021) doi:10.1093/mnras/stab052
Advance Access publication 2021 January 12

gzK-colour-selected star-forming galaxies in the *AKARI* NEP-Deep Field

Hyunjong Seo [1]★† Woong-Seob Jeong,[1,2] Hyunjin Shim,[3] Minjin Kim,[4] Jongwan Ko,[1,2] Jeonghyun Pyo,[1] Chris Pearson [5,6,7] Nagisa Oi [8] Tomotsugu Goto[9] and Takamitsu Miyaji [10,11]‡

[1]*Korea Astronomy and Space Science Institute (KASI), 776 Daedeok-daero, Yuseong-gu, Daejeon 34055, Republic of Korea*
[2]*Korea University of Science and Technology, 217 Gajeong-ro, Yuseong-gu, Daejeon 305-350, Republic of Korea*
[3]*Department of Earth Science Education, Kyungpook National University, 80 Daehakro, Buk-gu, Daegu 41566, Republic of Korea*
[4]*Department of Astronomy and Atmospheric Sciences, Kyungpook National University, Daegu 702-701, Republic of Korea*
[5]*RAL Space, STFC Rutherford Appleton Laboratory, Didcot, Oxfordshire OX11 0QX, UK*
[6]*School of Physical Sciences, The Open University, Milton Keynes MK7 6AA, UK*
[7]*Oxford Astrophysics, University of Oxford, Keble Road, Oxford OX1 3RH, UK*
[8]*Tokyo University of Science, 1-3 Kagurazaka, Shinjuku-ku, Tokyo 162-8601, Japan*
[9]*Institute of Astronomy, National Tsing Hua University, No. 101, Section 2, Kuang-Fu Road, Hsinchu 30013, Taiwan*
[10]*Instituto de Astronomía, Universidad Nacional Autónoma de México (UNAM), Km. 107 Carret. Tij.-Ens., Ensenada 22860, Mexico*
[11]*Leibniz Institut für Astrophysik Potsdam (AIP), An der Sternwarte 16, D-14482 Potsdam, Germany*

Accepted 2021 January 4. Received 2020 December 4; in original form 2020 August 24

ABSTRACT

We study the clustering property and physical parameters of *gzK*-colour-selected star-forming galaxies (sgzKs) based on the Canada–France–Hawaii Telescope surveys over 0.55 deg^2 in the *AKARI* North Ecliptic Pole-Deep Field. Two-point correlation functions for two magnitude-limited cases, $K_s < 21.1$ ($N = 234$) and $K_s < 21.5$ ($N = 428$), are estimated using a single power-law function with the fixed slope of 0.8. The bias factors of sgzKs with $K_s < 21.1$ and 21.5 are 5.79 ± 1.07 and 4.00 ± 0.67, respectively, representing that sgzKs with $z \sim 1.7$ reside in dark matter haloes more massive than 10^{13} M$_\odot$. We find that haloes hosting sgzKs with $K_s < 21.5$ evolve into haloes that host local massive galaxies with ∼6 L*. This suggests that sgzKs with $K_s < 21.5$ are likely to be predecessors of local massive galaxies. The evolutionary track of bias factor for host haloes of the bright sgzKs is similar to that of the bright passive extremely red objects, implying a possible connection between the two populations of galaxies. From the spectral energy distribution fitting, we estimate physical parameters and active galactic nucleus (AGN) contribution for 75 mid-infrared (MIR)-detected sgzKs with $K_s < 21.5$. The median values of stellar mass and star formation rate are 9.5×10^{10} M$_\odot$ and 162 M$_\odot$ yr^{-1}, respectively. MIR-detected sgzKs have a variety of AGN contributions ranging from 0 to 80 per cent. The number ratio of sgzKs with larger AGN contribution than 10 per cent is 30 per cent.

Key words: galaxies: evolution – galaxies: formation – galaxies: high-redshift.

1 INTRODUCTION

Studies show that the cosmic star formation rate (SFR) density peaks at $z \sim 2$ and decreases gradually towards lower redshifts (Gruppioni et al. 2013; Magnelli et al. 2013; Goto et al. 2015). Active galactic nucleus (AGN) accretion density also decreases with the passage of time since its peak at $z \sim 2$, representing the co-evolution of galaxy growth and AGN activity (Silverman et al. 2008; Madau & Dickinson 2014; Aird et al. 2015). Therefore, high-redshift galaxies, especially at around $z \sim 2$, are important to study the evolution of galaxies and AGN activities therein. To select high-redshift galaxies, photometric colour between optical and infrared (IR) bands is often used, including *BzK*-colour-selected galaxies (BzKs; Daddi et al. 2004), extremely red objects (EROs; Elston, Rieke & Rieke 1988), and dust-obscured galaxies (DOGs; Dey et al. 2008). Daddi et al. (2004) proposed two-colour selection technique based on the *B*, *z*, and *K* bands to classify star-forming and passive galaxies at $1.4 \leq z \leq 2.5$ (BzKs or BzK galaxies). Instead of the *B* band, the *g* band is often used (gzKs or gzK galaxies). Since then, many studies showed that *BzK*-colour selection method is efficient to select massive galaxies at $z > 1.4$ (Kong et al. 2006; Hayashi et al. 2007; Blanc et al. 2008; Bielby et al. 2012; Fang et al. 2012; Ishikawa et al. 2015). BzK galaxies at $z \sim 2$ are an important population to investigate the formation and evolution of galaxies in the present Universe.

Clustering analysis of galaxies is one of the useful methods to search for an evolutionary link among galaxy populations at different redshifts. In terms of the clustering analysis, previous studies suggested that BzKs could be candidates for the progenitors of local massive galaxies (Hayashi et al. 2007; Blanc et al. 2008). Other massive populations at high redshift, such as EROs (Kim et al. 2011; Palamara et al. 2013; Shin et al. 2017; Seo et al. 2019), DOGs (Brodwin et al. 2008), and sub-millimetre galaxies (SMGs; Wilkinson et al. 2017), have also been proposed as candidates for the progenitors of massive galaxies in the present Universe. In addition,

★ E-mail: hyunjongseo11@gmail.com
† Present address: 45, Gungdong-ro, Yuseong-gu, Daejeon 34137, Republic of Korea.
‡ On sabbatical leave from UNAM at AIP.

the correlation among these candidates has been studied in terms of the clustering property. Kong et al. (2006) proposed the possibility of evolutionary connection between EROs and BzKs based on their similar clustering properties. Brodwin et al. (2008) reported that the correlation length of faint DOGs (e.g. $\langle F_{24\,\mu m}\rangle \lesssim 0.53$ mJy) is similar to that of SMGs. Therefore, the comparison of clustering properties between BzKs and other populations with various redshifts is useful to understand the formation and evolution of galaxies.

Physical quantities of BzKs such as SFR, specific star formation rate (sSFR), IR luminosity (L_{IR}), stellar mass, and AGN contribution can be estimated by fitting spectral energy distributions (SEDs). Such quantities are useful to understand the evolution of BzKs. For example, in the galaxy evolution model, massive galaxies would pass both star formation-dominated phase and AGN-dominated phase after major mergers or smooth accretion (Bussmann et al. 2009; Dey & The NDWFS/MIPS Collaboration 2009; Narayanan et al. 2010; Bussmann et al. 2012). Therefore, the contribution of AGN to the IR luminosity in each BzK galaxy gives information about which phase is dominant for the BzK. While the X-ray data have usually been used to find out the number ratio of AGN-dominant BzKs (Daddi et al. 2005; Kong et al. 2006), such analysis depends on the sensitivity of X-ray data. It is known that photometry in mid-infrared (MIR) bands is a powerful alternative to select AGN candidates. Fang et al. (2012) investigated the number fraction of AGNs in gzK galaxies using the slope of SED at MIR bands. Krumpe et al. (2015) suggested that the AGN contribution determined by MIR SED fits is useful for the selection of AGN candidates. In the *AKARI* North Ecliptic Pole (NEP)-Deep Field, we can estimate the contribution of AGN to the IR luminosity using continuous IR coverage by nine photometric bands from 2.4 to 24 μm (Murata et al. 2013).

In this study, we investigate the clustering property and physical parameters of star-forming gzKs (sgzKs) based on the Canada–France–Hawaii Telescope (CFHT)/MegaCam and CFHT/WIRCam surveys (Oi et al. 2014) in the *AKARI* NEP-Deep Field (Matsuhara et al. 2006). Due to multiwavelength surveys and continuous IR coverage by *AKARI*, the NEP-Deep Field is one of the efficient sites for the study of galaxies. The correlation length and linear bias factor for sgzKs are estimated based on a two-point correlation function. In order to find possible evolutionary links among sgzKs, local galaxies, and other populations with various redshifts, we estimate the bias evolution for dark matter haloes hosting sgzKs. Photometric redshifts (photo-zs) for MIR-detected galaxies are estimated. For MIR-detected sgzKs with $1.4 \leq z \leq 2.5$, we estimate physical parameters and the contribution of AGN to the IR luminosity by fitting SEDs from optical to far-infrared (FIR) bands. This paper is structured as follows. We present photometric catalogues for the NEP-Deep Field and photometric colour criteria for the selection of sgzKs in Section 2. In Section 3, the clustering strength of sgzKs is estimated using the two-point correlation function, correlation length, and bias factor. In Section 4, the evolution of sgzKs is discussed based on the evolution of bias for host haloes. Physical parameters for MIR-detected sgzKs are estimated by fitting SEDs, and the result is discussed in comparison with the results from the previous studies. The study is summarized in the final section. Throughout the paper, we assume a flat universe with $(\Omega_M, \Omega_\Lambda, H_0) = (0.3, 0.7, \text{and } 70\ \text{km s}^{-1}\ \text{Mpc}^{-1})$. We use AB magnitude system unless otherwise specified.

2 DATA

2.1 Catalogues

The *AKARI* NEP-Deep Field covering ∼0.55 deg^2 area centred at $(\alpha_{2000}, \delta_{2000}) = (17^h55^m24^s, +66^\circ37'32'')$ is initiated by *AKARI*/IRC observations for the IR range from 2.4 to 24 μm (Matsuhara et al. 2006; Murata et al. 2013), which consists of nine photometric bands in three channels: NIR ($N2$, $N3$, $N4$), MIR–S ($S7$, $S9W$, $S11$), and MIR–L ($L15$, $L18W$, $L24$). CFHT/MegaCam u^* band covers the entire NEP-Deep Field with 5σ limiting magnitude of 24.6 mag (Takagi et al. 2012; Oi et al. 2014). CFHT/MegaCam covers an area of ∼1.03 deg^2 using the optical g', r', i', and z' bands that have 4σ detection limits of 26.7, 25.9, 25.1, and 24.1 mag, respectively (Oi et al. 2014). CFHT/WIRCam covers an area of ∼0.64 deg^2 using near-infrared (NIR) Y, J, and K_s bands that have 4σ detection limits of 23.4, 23.0, and 22.7 mag, respectively (Oi et al. 2014). The area of CFHT/MegaCam includes that of CFHT/WIRCam (Fig. 1). *Herschel*/PACS surveys at 100 and 160 μm whose 50 per cent completeness levels are 6 and 19 mJy, respectively (Pearson et al. 2019). *Herschel*/SPIRE surveys at 250, 350, and 500 μm whose 50 per cent completeness levels are 16, 23, and 19 mJy, respectively (Pearson et al. 2017). For the estimation of photo-z, two additional data sets in the NEP field were used. FLAMINGOS covers an area of 5.1 deg^2 with the J and H bands that have 5σ depths of ∼21.6 and ∼21.3 mag, respectively (Jeon et al. 2014). *Spitzer*/IRAC covers an area of 7.04 deg^2 with 3.6 and 4.5 μm bands that have 1σ depths of 1.29 and 0.79 μJy, respectively (Nayyeri et al. 2018).

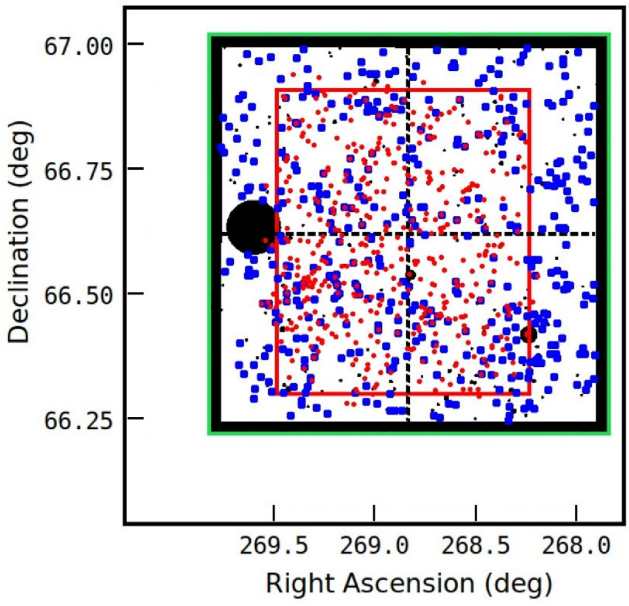

Figure 1. Coverage of CFHT survey and sgzKs. The green and black boxes represent the areas for WIRCam and MegaCam surveys, respectively. Large blue symbols represent sgzKs with $K_s < 21.5$. Red dots show X-ray sources by *Chandra* observations (Krumpe et al. 2015). For convenience, cross-matching between sgzKs and X-ray sources is conducted within the red box. Black regions within the green box are excluded from the study. The largest black circular area with 400 arcsec in diameter is excluded because of scattered light by a planetary nebula NGC 6543. Other black circles represent the masked regions around stars. To reduce edge effect, 0.°025 from each side is excluded. Thus, an effective area for the study, white region within the green box, is approximately 0.55 deg^2. Four sub-regions divided by the dashed lines are defined to investigate an effect of cosmic variance on the number count and clustering analysis.

2.2 gzK galaxies

Daddi et al. (2004) used the B, z, and K bands to select star-forming and passive galaxies at $1.4 \leq z \leq 2.5$ by two-colour selection criteria. Instead of the B band, we used the CFHT/MegaCam g' band to adopt

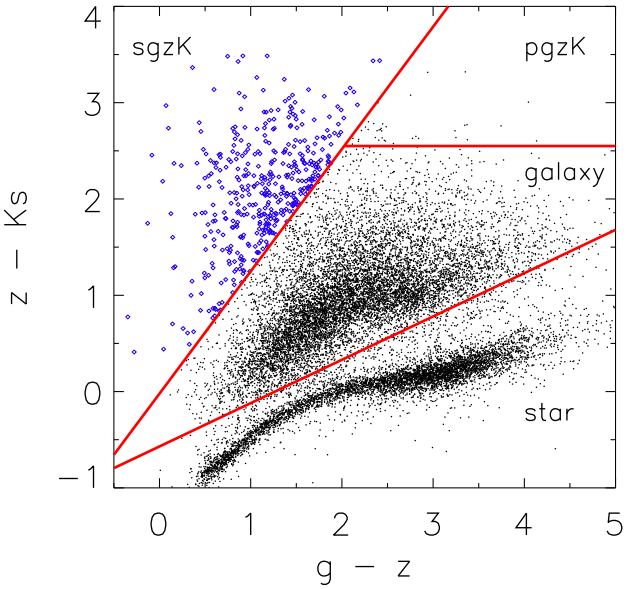

Figure 2. *gzK*-colour diagram for CFHT objects with $K_s < 21.5$ in the NEP-Deep Field. Three solid lines correspond to the criteria in equations (1)–(3). sgzKs with $K_s < 21.5$ denoted by the blue diamond ($N = 428$) are used in this study.

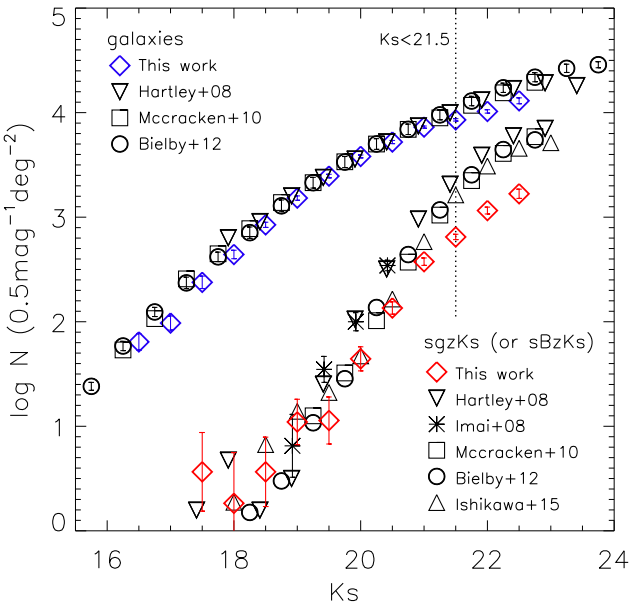

Figure 3. Number counts of galaxies and sgzKs (upper and lower groups, respectively). Blue and red diamonds are K_s-band completeness corrected number counts for galaxies and sgzKs, respectively, in this study. Other symbols are the results for galaxies and sgzKs (or sBzKs) in the literature (Hartley et. al. 2008; Imai et. al. 2008; McCracken et. al. 2010; Bielby et. al. 2012; Ishikawa et. al. 2015). The vertical dotted line shows the magnitude cut for sgzKs in this study, which corresponds to ∼83 per cent completeness level of the K_s band.

BzK selection method in the *AKARI* NEP-Deep Field. Since *BzK* filter set in Daddi et al. (2004) differs from CFHT *gzK* filter set in this study, filter correction is required to appropriately apply BzK selection technique to this study. Bielby et al. (2012) and Arcila-Osejo & Sawicki (2013) investigated CFHT filter set version of the BzK selection method. We tested both versions, and found that they give almost similar results. Arcila-Osejo & Sawicki (2013) presented *gzK*-colour cuts that were transformed from the *BzK*-colour cuts in Daddi et al. (2004). We adopted the *gzK*-colour cuts in this study. The criteria of *gzK* selection with the CFHT filter set are as follows:

$$(z - K_s) - 1.27(g - z) \geq -0.022, \quad (1)$$

$$(z - K_s) - 1.27(g - z) < -0.022 \cap (z - K_s) > 2.55, \quad (2)$$

$$(z - K_s) - 0.45(g - z) \leq -0.57, \quad (3)$$

where three equations represent the criteria for selecting sgzKs, passive gzKs (pgzKs), and stars, respectively. In this study, we restrict our sample to sgzKs because a small number of pgzKs are found in the CFHT catalogue of the NEP-Deep Field. Fig. 2 shows *gzK* colour for the CFHT objects with $K_s < 21.5$ in the NEP-Deep Field. The criteria in equations (1)–(3) divide the *gzK*-colour diagram into four regions. Upper two regions correspond to sgzKs and pgzKs, respectively, while lower two regions correspond to galaxies at $z <$ 1.4 and stars, respectively. sgzKs with $K_s < 21.5$ denoted by the blue diamond ($N = 428$) are used in this study to investigate clustering property. Among them, MIR-detected sgzKs are used to estimate physical parameters.

Number counts of K_s-detected galaxies and sgzKs in the NEP-Deep Field after the correction of K_s-band completeness are presented in Fig. 3. In order to count galaxies and sgzKs, star candidates are excluded by both $u^*g'JK_s$ colour criteria and stellarity (>0.8) given in Oi et al. (2014). Although star candidates can be excluded by the *gzK*-colour selection criteria (Fig. 2), we further adopted star separation criteria of Oi et al. (2014) to exclude stars clearly from sgzKs. The uncertainty of number count is determined by the combination of two kinds of errors. First, we estimated Poisson error ($=\sqrt{N}$) for each bin. Secondly, we considered the error due to cosmic variance. For this error, we used four sub-regions presented in Fig. 1. Number counts were estimated four times separately after excluding each of the sub-regions in turn. A standard deviation of the four number counts can be treated as the uncertainty of number count due to cosmic variance. The two kinds of errors were added quadratically to estimate the uncertainty of number count. In this study, the analysis of sgzKs is conducted up to $K_s < 21.5$, which corresponds to ∼83 per cent completeness level of the K_s band (Oi et al. 2014). The number count of galaxies with $K_s < 21.5$ in this study is roughly comparable to those in the literature, while that of sgzKs with $K_s < 21.5$ is detached from those in the literature at fainter magnitude. One possible reason is that the filter transformation to the original filter set in Daddi et al. (2004) varies depending on the study, which results in different number counts of sgzKs. In addition, the number count of sgzKs is related with the depths of the g' and z' bands as well as that of the K_s band.

3 CLUSTERING ANALYSIS

3.1 Two-point correlation function

The two-point correlation function for sgzKs was estimated by the estimator in Landy & Szalay (1993), which describes the excess probability of observed sgzK pairs compared to randomly distributed artificial object pairs at a specific angular separation, as presented below:

$$\omega_{\rm obs}(\theta) = \frac{DD(\theta) - 2DR(\theta) + RR(\theta)}{RR(\theta)}, \quad (4)$$

where $DD(\theta)$, $DR(\theta)$, and $RR(\theta)$ represent the normalized number of sgzK–sgzK, sgzK–random, and random–random pairs, respectively. For the estimation of two-point correlation function, we generated a simulated catalogue that consists of randomly distributed artificial coordinates with 100 times more numerous than the observed sgzKs. The simulated catalogue covers the same area where sgzK selection is conducted (i.e. the white region within the green box in Fig. 1). Two-point correlation function was estimated in the angular scale up to $0\overset{\circ}{.}375$ corresponding to half of a side of the K_s-band coverage. The angular scale is divided into six bins, and the uncertainty of two-point correlation function in each bin is estimated by jackknife error as follows. K_s-band coverage is divided into 16 square-shaped sub-regions (0.2×0.2 deg^2 per each sub-region), and two-point correlation function is estimated separately by excluding each of 16 sub-regions in turn. Then, the jackknife error is estimated as follows (Nikoloudakis, Shanks & Sawangwit 2013; Kim et al. 2014):

$$\sigma^2_{\rm JK}(\theta) = \sum_{i=1}^{N} \frac{DR_i(\theta)}{DR(\theta)} [\omega_i(\theta) - \omega(\theta)]^2, \tag{5}$$

where $DR_i(\theta)$ and $\omega_i(\theta)$ are the non-normalized number of sgzK–random pairs and the two-point correlation function, respectively, when the i-th sub-region is excluded. N equals 16 representing the total number of sub-regions.

The observed two-point correlation function $\omega_{\rm obs}(\theta)$ is corrected for an underestimation due to a finite coverage of the observation data. The correction is conducted by adding an integral constraint (IC; Groth & Peebles 1977) as follows:

$$\omega(\theta) = \omega_{\rm obs}(\theta) + {\rm IC}. \tag{6}$$

With the assumption of a single power-law correlation function $\omega(\theta) = A_\omega \theta^{-\delta}$, IC is expressed by the formalism in Roche et al. (1999) as

$${\rm IC} = \frac{\Sigma_i [RR(\theta_i)\omega(\theta_i)]}{\Sigma_i RR(\theta_i)}, \tag{7}$$

where $RR(\theta_i)$ is the non-normalized number of random–random pairs. Combined with equation (7), equation (6) becomes

$$\omega_{\rm obs}(\theta) = A_\omega \left[\theta^{-\delta} - \frac{\Sigma_i [RR(\theta_i)\theta_i^{-\delta}]}{\Sigma_i RR(\theta_i)}\right]. \tag{8}$$

The observed two-point correlation function $\omega_{\rm obs}(\theta)$ is fitted by equation (8) to obtain the corrected two-point correlation function $\omega(\theta)$. We conducted the fit by fixing a slope parameter δ to 0.8. Since δ is sensitive to the sample size, constraining the slope δ is not effective because of the small number of sgzK galaxies. The result with fixed δ is useful for direct comparison with previous studies since many studies assumed the slope parameter δ fixed to 0.8 (Kong et al. 2006; Hayashi et al. 2007; Blanc et al. 2008; Hartley et al. 2008; Ishikawa et al. 2015). The least-squares fit procedure in MPFIT[1] (Markwardt 2009) was used to determine A_ω. The two-point correlation functions for sgzKs with $K_s < 21.1$ and 21.5 are presented in Fig. 4. Ishikawa et al. (2015) reported that the two-point correlation function of sgzKs at small angular scale ($\theta \lesssim 0\overset{\circ}{.}01$) has a steeper slope compared to that at large angular scale, which represents the difference of contributions from the one-halo term (pairs of sgzKs in the same halo) and the two-halo term (pairs of sgzKs in different haloes) as predicted from the analysis by the dark matter halo model. However, such characteristic is unclear in Fig. 4 due to the small number of sgzK galaxies. The results of clustering analysis for the two magnitude-limited sgzKs are listed in Table 1. In Fig. 5, the amplitudes of two-point correlation functions for sgzKs are presented together with the results in the literature. For the estimation of the error, we considered the effect of cosmic variance. For this, we used four sub-regions presented in Fig. 1. Two-point correlation functions were estimated four times separately after excluding each of the sub-regions in turn. A standard deviation of the four two-point correlation functions can be treated as the uncertainty of two-point correlation function due to cosmic variance. It was added quadratically in the estimation of the error of two-point correlation function. As shown in Fig. 5, our result is comparable to the previous studies. In addition to the results in the literature, our result shows K_s-band magnitude dependence of the clustering strength.

[1] https://www.physics.wisc.edu/~craigm/idl/fitting.html

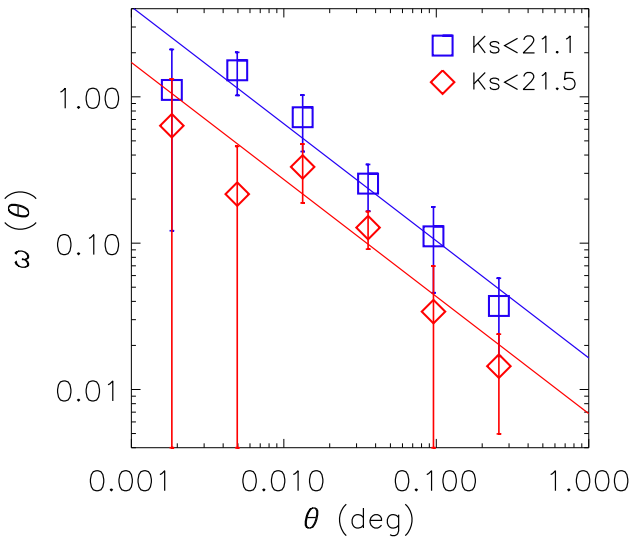

Figure 4. Two-point correlation functions for two magnitude-limited sgzKs. The error in each bin is estimated by jackknife method. Solid lines are the fitted single power-law functions, $\omega(\theta) = A_\omega \theta^{-\delta}$, with the fixed δ of 0.8. The result of clustering analysis is presented in Table 1.

3.2 Correlation length

Three-dimensional two-point correlation function can be expressed as a power-law form:

$$\xi(r) = \left(\frac{r}{r_0}\right)^{-\gamma}, \tag{9}$$

where r_0 is a correlation length and $\gamma = 1 + \delta$. If the redshift distribution of sgzKs is available, the correlation length r_0 can be estimated from the two-dimensional two-point correlation function by Limber's equation (Limber 1953):

$$A_\omega = \frac{C_\gamma H_0 r_0^\gamma}{c} \frac{\int_0^\infty ({\rm d}N/{\rm d}z)^2 r(z)^{1-\gamma} E(z) {\rm d}z}{N^2}, \tag{10}$$

where

$$C_\gamma = \frac{\Gamma(1/2)\Gamma[(\gamma-1)/2]}{\Gamma(\gamma/2)}, \tag{11}$$

$$r(z) = \frac{c}{H_0} \int_0^z \frac{1}{E(z')} {\rm d}z', \tag{12}$$

$$E(z) = [\Omega_{\Lambda,0} + \Omega_{{\rm m},0}(1+z)^3]^{1/2}, \tag{13}$$

N is the total number of sgzKs, $r(z)$ is a transverse comoving distance, and Γ is a mathematical gamma function. The uncertainty of A_ω is

Table 1. Clustering analysis of sgzKs. $\langle z \rangle$ represents the median photo-z (see Fig. 6).

Magnitude limit	N	$\langle z \rangle$	A_ω ($\times 10^{-3}$)	δ	r_0 (h^{-1}Mpc)	b	$M_{\rm halo}$ ($\times 10^{13}$M$_\odot$)
$K_{\rm s} < 21.1$	234	1.681	16.43 ± 6.10	0.8	13.98 ± 2.88	5.79 ± 1.07	$8.90^{+4.74}_{-3.76}$
$K_{\rm s} < 21.5$	428	1.721	6.84 ± 2.28	0.8	9.13 ± 1.69	4.00 ± 0.67	$2.99^{+1.69}_{-1.31}$

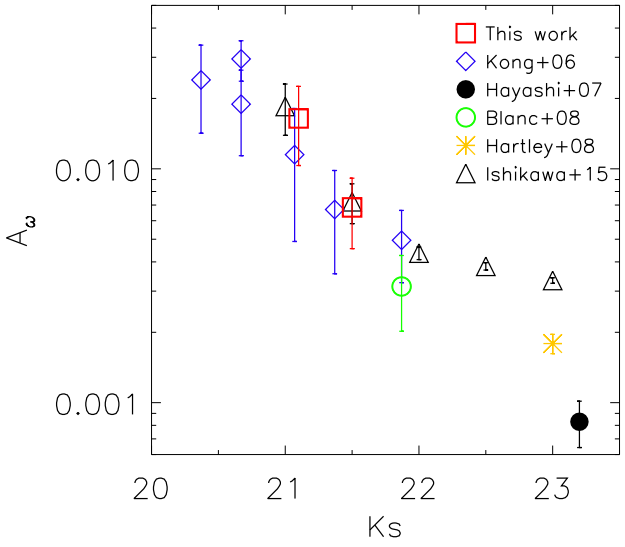

Figure 5. The amplitude of two-point correlation function as a function of $K_{\rm s}$-band limiting magnitude. Red squares are the results for sgzKs with $K_{\rm s}$ < 21.1 and 21.5 in this study. Other symbols are the results for sgzKs (or sBzKs) in the literature. Red squares and other symbols show that clustering strength is dependent on the $K_{\rm s}$-band magnitude.

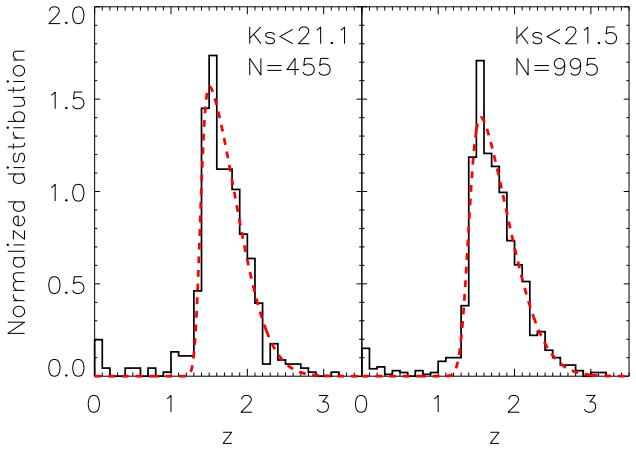

Figure 6. Photo-z distributions for two magnitude-limited sgzKs (black histograms). They are extracted from AEGIS/NMBS and COSMOS/NMBS catalogues in Whitaker et al. (2011). To select sgzKs, we used the same gzK-colour selection criteria as those applied to the NEP-Deep Field. Black histograms are fitted using equation (14), resulting in red dashed histograms. After scaling the area to be 1, the red dashed histograms are applied to dN/dz in equation (10). The best-fitting parameters (σ, μ, α) of equation (14) for the two magnitude-limited sgzKs are (0.445, 1.381, 7.873) and (0,485, 1.393, 5.720), respectively. The median redshifts of the red dashed histograms are 1.681 and 1.721, respectively.

translated into the uncertainty of correlation length through the error propagation formula. dN/dz is the redshift distribution of sgzKs, which was extracted from publicly available catalogues. As part of the NEWFIRM Medium-Band Survey (NMBS), Whitaker et al. (2011) presented NIR medium-bandwidth photometry catalogues for AEGIS and COSMOS fields, each of which covers 0.21 deg^2. Although the field coverage is small, with the help of five filters over the spectral range 1–1.8 μm, the catalogues present precise photo-z with $\sigma_{\Delta z/(1+z)} = 0.017$ and 0.008 for AEGIS and COSMOS fields, respectively. The same gzK-colour selection criteria were adopted for the selection of sgzKs in the catalogues of Whitaker et al. (2011), resulting in black histograms in Fig. 6. The histograms confirm that gzK-colour criteria are efficient to select galaxies with $z > 1.4$. The black histogram is fitted by the combination of Gaussian and the error function as follows:

$$f(z) = \frac{1}{\sqrt{2\pi\sigma^2}} \exp\left(-\frac{(z-\mu)^2}{2\sigma^2}\right)\left[1 + {\rm erf}\left(\frac{\alpha}{\sqrt{2}}\frac{(z-\mu)}{\sigma}\right)\right], \quad (14)$$

where erf is the error function, and α represents a skewness of the histogram. Equation (14) becomes Gaussian when $\alpha = 0$. Red dashed histograms in Fig. 6 represent the fitted redshift distributions, and they are applied to dN/dz in equation (10).

Fig. 7 shows the correlation length of sgzKs with $K_{\rm s} < 21.5$ along with the results for other populations with various redshifts in the literature. As shown, the correlation length of sgzKs is comparable to those of EROs with $K_{\rm s} < 20.9$ (Seo et al. 2019) and SMGs at $z = 2$–3 (Wilkinson et al. 2017). It is also comparable to those of ultraluminous IR galaxies (ULIRGs) at comparable redshift (Farrah

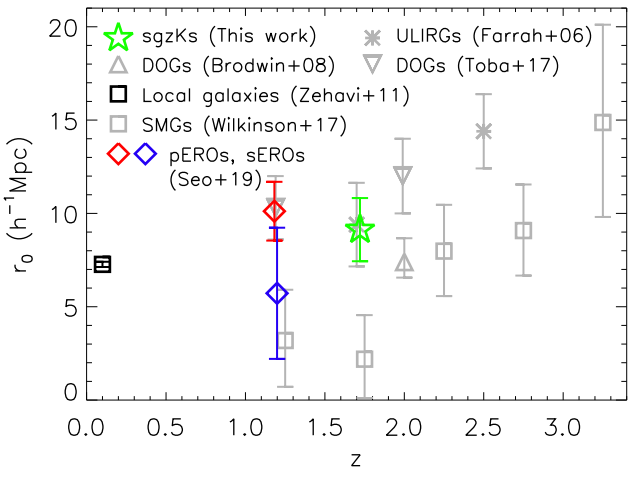

Figure 7. Correlation length as a function of redshift. The green star symbol is sgzKs with $K_{\rm s} < 21.5$ in this study. Red and blue diamonds represent pEROs and star-forming EROs (sEROs) with $K_{\rm s} < 20.9$, respectively (Seo et al. 2019). Grey squares show SMGs (Wilkinson et al. 2017). Downward triangles show DOGs with $3.0 < F_{22\ \mu{\rm m}} < 5.0$ mJy (Toba et al. 2017), and the upward triangle represents DOGs with $F_{24\ \mu{\rm m}} > 0.3$ mJy (Brodwin et al. 2008). Asterisks are ULIRGs with stellar mass $\gtrsim 10^{11}$ M$_\odot$ and SFR $\gtrsim$200 M$_\odot$ yr^{-1} (Farrah et al. 2006). The black square shows local galaxies at $0.02 < z < 0.2$ with $M_r < -21.5$, where ∼73 per cent of the sources are red galaxies (Zehavi et al. 2011).

et al. 2006), DOGs with $3.0 < F_{22\,\mu m} < 5.0$ mJy (Toba et al. 2017), and DOGs with $F_{24\,\mu m} > 0.3$ mJy (Brodwin et al. 2008). In terms of the correlation length, local red galaxies in Zehavi et al. (2011) are also comparable to sgzKs. In addition to EROs, SMGs, and DOGs, sgzKs are known as possible predecessors of local massive galaxies. Thus, we investigated the expected evolution of sgzKs using a bias factor.

3.3 Bias

In order to explain clustering of galaxies and its evolution, a linear bias factor, a parameter representing the difference between galaxy distribution and underlying matter distribution, is often introduced. The linear bias factor b of sgzKs at a scale of $8\,h^{-1}$ Mpc is expressed as follows:

$$b = \frac{\sigma_{8,\mathrm{sgzK}}}{\sigma_8(z)}. \tag{15}$$

The rms fluctuation of sgzK distribution $\sigma_{8,\mathrm{sgzK}}$ (Peebles 1980) and that of underlying matter distribution at a given redshift $\sigma_8(z)$ can be expressed as follows:

$$\sigma_{8,\mathrm{sgzK}} = \sqrt{J_2(\gamma)\left(\frac{r_0}{8\,h^{-1}\,\mathrm{Mpc}}\right)^{\gamma}} \tag{16}$$

and

$$\sigma_8(z) = \sigma_8(0)D(z), \tag{17}$$

where

$$D(z) = g(z)/[g(0)(1+z)], \tag{18}$$

$$g(z) = \frac{5}{2}\Omega_\mathrm{m}\left[\Omega_\mathrm{m}^{4/7} - \Omega_\Lambda + \left(1+\frac{\Omega_\mathrm{m}}{2}\right)\left(1+\frac{\Omega_\Lambda}{70}\right)\right]^{-1}, \tag{19}$$

$$\Omega_\mathrm{m} = \frac{\Omega_{\mathrm{m},0}(1+z)^3}{E^2(z)}, \quad \Omega_\Lambda = \frac{\Omega_{\Lambda,0}}{E^2(z)}; \tag{20}$$

the present rms mass fluctuation is $\sigma_8(0) = 0.83$ (Planck Collaboration XVI 2014) and $J_2(\gamma) = 72/[2^\gamma(3-\gamma)(4-\gamma)(6-\gamma)]$. Fig. 8 shows the bias factor of sgzKs along with those of other populations in the literature.[2] The bias of sgzKs with $K_\mathrm{s} < 21.5$ is larger than those of SMGs with $z < 2$, while it is similar to those of ULIRGs at comparable redshift, EROs, DOGs with $z \sim 1.2$, and SMGs with $z = 2$–3. Galaxies and their host dark matter haloes can be connected through the correlation length or the bias factor under the assumption that each dark matter halo is occupied by a single galaxy. Therefore, in order to find present-day descendants of high-redshift galaxy populations, we can use a redshift evolution of the bias for dark matter haloes hosting high-redshift galaxies. For example, Hickox et al. (2012) and Wilkinson et al. (2017) investigated the evolution of either correlation length or bias for the haloes of SMGs to find an evolutionary link between high-redshift SMGs and local galaxies. Seo et al. (2019) also used the same method to find descendants of EROs. Thus, we investigated the evolution of bias for dark matter haloes hosting sgzKs with $K_\mathrm{s} < 21.5$. By the ellipsoidal collapse model, Mo & White (2002) estimated the bias for dark matter haloes

[2]The bias factors of ULIRGs are estimated in this study using equation (15) combined with the correlation lengths and central redshifts given in Farrah et al. (2006). The bias factors of SMGs are re-estimated by adopting $\sigma_8 = 0.83$, resulting in ∼9 per cent larger compared to those in Wilkinson et al. (2017).

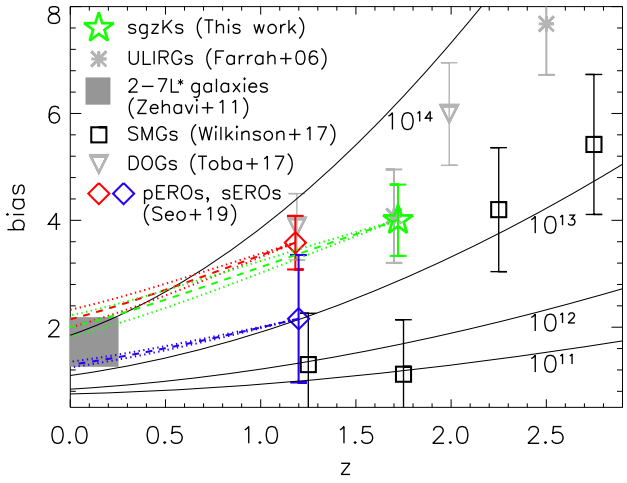

Figure 8. Bias factor as a function of redshift. Black squares show SMGs (Wilkinson et al. 2017). The grey shaded region shows the range of bias for local galaxies with 2–7 L* (Zehavi et al. 2011). Other symbols are the same as those in Fig. 7. The various lines show the evolution of bias for dark matter haloes estimated by equation (21). Solid lines represent the results assuming fixed halo masses that are labelled in solarmass unit, while dashed lines show the results taking into account the mass growth of haloes. To calculate the mass growth of haloes at a given redshift, we considered the mean growth rate (upper dotted line of each symbol) and the median growth rate (lower dotted line of each symbol) in equations (23) and (24), respectively. The dotted lines explicitly show the difference of the two mass growth rates. The dashed line represents the average of the two dotted lines.

with mass M at a given redshift as follows:

$$b(M,z) = 1 + \frac{1}{\delta_\mathrm{c}}\left[\nu'^2 + b\nu'^{2(1-c)} - \frac{\nu'^{2c}/\sqrt{a}}{\nu'^{2c} + b(1-c)(1-c/2)}\right], \tag{21}$$

where

$$\nu' = \sqrt{a}\nu \quad \text{with} \quad \nu = \frac{\delta_\mathrm{c}}{\sigma(R)D(z)}, \tag{22}$$

$a = 0.707$, $b = 0.5$, $c = 0.6$, the critical overdensity is $\delta_\mathrm{c} = 1.686$ (Sheth, Mo & Tormen 2001), and $\sigma(R)$ is the variance of density field fluctuation.[3] To trace the bias of haloes over redshift, we calculated halo mass M at a given redshift using the formalism for mass growth rate of a halo. Fakhouri, Ma & Boylan-Kolchin (2010) suggested two kinds of mass growth rates, mean growth rate $\langle \dot{M} \rangle_\mathrm{mean}$ and median growth rate $\langle \dot{M} \rangle_\mathrm{median}$, as follows:

$$\langle \dot{M} \rangle_\mathrm{mean} = 46.1\ \mathrm{M_\odot\ yr^{-1}}\left(\frac{M}{10^{12}\ \mathrm{M_\odot}}\right)^{1.1}(1+1.11z)E(z) \tag{23}$$

and

$$\langle \dot{M} \rangle_\mathrm{median} = 25.3\ \mathrm{M_\odot\ yr^{-1}}\left(\frac{M}{10^{12}\ \mathrm{M_\odot}}\right)^{1.1}(1+1.65z)E(z), \tag{24}$$

where the former is larger than the latter. We estimated each mass growth rate separately, and took their average as the mass growth rate of the halo with M at a given z. In Fig. 8, dashed

[3]The procedure for the estimation of bias of dark matter haloes is the same as that in our previous study. The detailed explanation for equation (21) is presented in section 4.3 of Seo et al. (2019).

lines represent the evolution of bias for haloes, which are the results considering the mass growth of haloes. On the other hand, solid lines show the evolution of bias for haloes with fixed halo mass.

4 DISCUSSION

4.1 The evolution of sgzK galaxies

Seo et al. (2019) reported that the dark matter haloes that host EROs with $K_s < 20.9$ at $z \sim 1.2$ evolve into haloes hosting local massive galaxies with 2–7 L* (grey shaded region in Fig. 8). The same as EROs in Seo et al. (2019), the dashed line from sgzK is also connected to the grey shaded region, which represents that haloes hosting sgzKs with $K_s < 21.5$ at $z \sim 1.7$ evolve into haloes hosting local massive galaxies with ∼6 L*. This suggests that sgzKs are also likely possible predecessors of local massive galaxies. In addition, there may be a possible evolutionary connection between sgzKs and passive EROs (pEROs) since their bias factors are comparable. The evolutionary track of bias factor for host haloes of sgzKs with $K_s < 21.5$ is especially similar to that of pEROs with $K_s < 20.9$. They have comparable number densities. Number densities of sgzKs[4] and pEROs are 5.3×10^{-5} and 7.1×10^{-5} Mpc^{-3}, respectively. Based on the median redshifts of sgzKs and pEROs, cosmic time interval between them is ∼1.38 Gyr. In order to evolve passively from sgzKs to pEROs, star formation of sgzKs should be quenched within 1.38 Gyr. For example, Mancini et al. (2015) suggested that star formation of massive galaxies with $M_* \geq 10^{11}$ M$_\odot$ at $1.4 \leq z \leq 2$ can be quenched in short time-scales (<1 Gyr). Therefore, the evolutionary connection between sgzKs and pEROs is a plausible scenario.

The evolution of star-forming galaxies at high redshift has been studied in the literature. Magliocchetti et al. (2014) collected the results of clustering analyses for star-forming galaxies with SFR ∼ 30–1000 M$_\odot$ yr^{-1} from the literature, and homogenized the collected results for direct comparison. They found that correlation lengths (or minimum halo masses) of star-forming galaxies at high redshift ($z \gtrsim 2$) are much larger than those of low-redshift ($z \lesssim 1$) star-forming galaxies, representing that low-redshift star-forming galaxies reside in less massive dark matter haloes compared to high-redshift star-forming galaxies as predicted in the downsizing scenario. They further reported that clustering properties (e.g. minimum halo masses) of high-redshift star-forming galaxies are comparable to those of low-redshift ($z \lesssim 1.5$) passive galaxies with stellar masses of 10^{11}–10^{12} M$_\odot$, representing that there is an evolutionary connection between high-redshift star-forming galaxies and $z \lesssim 1.5$ massive passive galaxies; i.e. massive star-forming galaxies at $z \gtrsim 2$ evolve into $z \lesssim 1.5$ massive passive galaxies after a characteristic time-scale of ∼1 Gyr. Our argument is consistent with their result. The evolution of gzKs (or BzKs) has been studied in the literature. Kong et al. (2006) suggested the possibility of an evolutionary link between EROs and BzKs due to their stronger clustering properties than generic galaxies at each redshift. Blanc et al. (2008) estimated the bias factor for BzKs and the bias evolution for dark matter haloes, and suggested that BzKs with $K_{Vega} < 20$ could be progenitors of local galaxies with $\gtrsim$1 L*. As shown in Fig. 5, because the clustering strength of sgzKs depends on the K_s magnitude, halo mass of local descendants would vary with the K_s magnitude of sgzKs. Hayashi et al. (2007) also made the point that halo mass of present-day descendants of star-forming BzKs (sBzKs) depends on the K-band brightness of sBzKs.

4.2 SED fitting

As shown in Fig. 7, the clustering strength of sgzKs is similar to those of some massive galaxy populations with various redshifts, implying possible evolutionary connections among them. In order to understand the evolution of sgzKs, we investigated physical quantities such as stellar mass, IR luminosity, SFR, and AGN contribution by fitting SED, using multiwavelength data in the NEP-Deep Field. Photo-z was estimated using the LEPHARE code[5] (Arnouts et al. 1999; Ilbert et al. 2006) with two sets of SED templates. 31 templates from Ilbert et al. (2009) describe elliptical, spiral, and starburst galaxies, while 30 templates in Salvato et al. (2009) mainly include AGN or hybrid templates that describe various portions of AGN component in the host galaxies. Basically, for the estimation of photo-z, eight CFHT and five *AKARI* bands were used. In addition, if available, the FLAMINGOS J and H bands (Jeon et al. 2014) and the *Spitzer*/IRAC 3.6 and 4.5 μm bands (Nayyeri et al. 2018) were added to improve the accuracy of photo-z. As a result, 61 SED templates were fitted to 17 bands from u^* to *S9W* for the estimation of photo-z. Extinction laws in Prevot et al. (1984) and Calzetti et al. (2000) were adopted with various $E(B-V)$s from 0 to 1.0 with the interval of 0.05. Photo-z was estimated for MIR-detected galaxies with a robust optical counterpart. When there are multiple optical candidates for a single MIR galaxy (Murata et al. 2013), we used a likelihood ratio analysis (LR analysis; Sutherland & Saunders 1992) to select a reliable optical counterpart. LR analysis considers both the magnitude in optical band (r' band) and the positional offset at the same time. We estimated a reliability R (Sutherland & Saunders 1992) for each optical candidate separately to find out which optical candidate is the most dominant contributor to a given longer wavelength band.[6] If multiple optical candidates are matched with a single MIR galaxy (Murata et al. 2013), we adopted the galaxy only when the reliability of the optical candidate is $R \geq 0.8$. Among MIR-detected galaxies with a robust optical counterpart, 572 galaxies have spectroscopic redshift (spec-z) data from at least two emission or absorption lines. Spec-z data were obtained based on the surveys by MMT/Hectospec, WIYN/Hydra (Shim et al. 2013), Keck/DEIMOS, GTC, Subaru/FMOS, and *AKARI*/SPICY (Ohyama et al. 2018). The 572 MIR-detected galaxies were used to estimate a systematic magnitude offset between photometric data and the best-fitting SED at spec-z. They were also used to check the accuracy of photo-z. In Fig. 9, photo-zs of 572 MIR-detected galaxies are compared with spec-zs. There are 30 photo-z outliers. Moreover, photo-zs of a few sgzKs are biased to higher redshift as shown by the red squares in Fig. 9. Therefore, we further applied additional sample selection criteria to reduce photo-z outliers. First, three outliers with photo-$z \gtrsim 2.5$ have a common feature in their optical SEDs: large photometric colour between the u^* and g' bands and a relatively flat SED between the g' and z' bands. The spectral break feature between

[4]In the right-hand panel of Fig. 6, 87 per cent of sgzKs with $K_s < 21.5$ (black histogram) in the NMBS catalogue are located at $1.4 \leq z \leq 2.5$. Therefore, to estimate the number density of sgzKs, we adopted the assumption that among 428 sgzKs with $K_s < 21.5$ in the NEP-Deep Field, 372 sgzKs (i.e. 87 per cent) are located at $1.4 \leq z \leq 2.5$.

[5]http://www.cfht.hawaii.edu/∼arnouts/lephare.html

[6]The detailed procedure of LR analysis for the NEP-Deep Field and the definition of the reliability R are presented in our previous study (see section 3 in Seo et al. 2018).

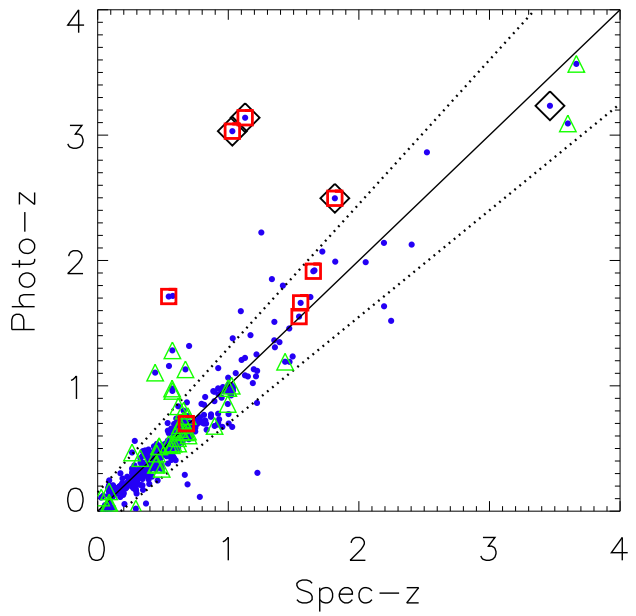

Figure 9. Photo-z is compared with spec-z for 572 MIR-detected galaxies (blue dots). Red squares are objects classified as sgzKs. Dotted lines represent photo-z = spec-z $\pm$ 0.15(1 + spec-z). Black diamonds show objects with a spectral break feature between the u^* and g' bands (see Section 4.2 for details). Green triangles show objects without u^*-band data. After excluding objects denoted by the black diamond and green triangle, the number of objects results in $N = 528$. A standard deviation of $\Delta z/(1+z)$ is $\sigma_{\Delta z/(1+z)} = 0.081$. Outlier rate is $\eta = 3.8$ per cent, where η defines the number ratio of objects located outside the dotted lines.

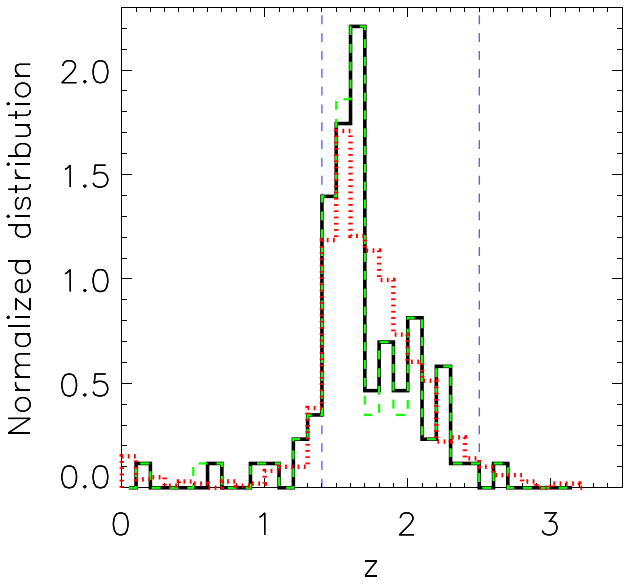

Figure 10. Redshift distributions for sgzKs with $K_s < 21.5$. The black histogram shows photo-z distribution of 86 MIR-detected sgzKs in the NEP-Deep Field. Photo-zs of a few sgzKs were replaced by spec-zs (green dashed histogram). We restrict our sample to MIR-detected sgzKs with $1.4 \leq z \leq 2.5$ (i.e. green dashed histogram between vertical dashed lines) for the estimation of physical parameters, which results in $N = 75$ (72 photo-zs and 3 spec-zs). The median redshift of 75 MIR-detected sgzKs is 1.645. For comparison, photo-z distribution of sgzKs with $K_s < 21.5$ in the NMBS catalogue (i.e. black histogram in the right-hand panel of Fig. 6) is presented (red dotted histogram). Histograms are normalized such that the area equals 1.

the u^* and g' bands is often misinterpreted as Lyman Break (rest-frame 912 Å), which results in photo-z around 3. So, we excluded such objects by introducing colour criteria as follows: $u^* - g' > 1.2$ and $u^* - g' > 3(g' - z')$ (four black diamonds in Fig. 9). Secondly, u^*-band data seem to be important to obtain an accurate photo-z. 7 out of 30 outliers do not have u^*-band data. So, the objects without u^*-band data were excluded (40 green triangles in Fig. 9). After that, the number of objects in Fig. 9 results in $N = 528$. Photo-z accuracy is $\sigma_{\Delta z/(1+z)} = 0.081$, and outlier rate is $\eta = 3.8$ per cent. The exclusion criteria mentioned here were also applied to the selection of MIR-detected sgzKs.

To investigate physical quantities of sgzKs, we imposed additional constraints for the selection of sgzKs. *AKARI*/IRC consists of nine photometric bands in three channels. To ensure continuous coverage in IR bands, we selected sgzKs that are detected in at least one band of each channel. Redshift distributions for sgzKs with $K_s <$ 21.5 are presented in Fig. 10. The black histogram represents the photo-z distribution of 86 MIR-detected sgzKs in the NEP-Deep Field, while the red dotted histogram represents that of sgzKs in the NMBS catalogue. In spite of their different peak positions, the overall shape of the two histograms is similar. As expected from the *gzK*-colour selection criteria, most of the sgzKs in the two histograms are located at $z > 1.4$. In the black histogram, the contaminants from lower redshift ($z < 1.4$) are about 10 per cent, which is comparable to the value of 10–13 per cent in Daddi et al. (2004). In addition, the shape of the black histogram at higher redshift (e.g. $z > 2$) is comparable to that of the red dotted histogram. Thus, there seems to be no catastrophic photo-z error in the majority of sgzKs. If available, photo-zs of sgzKs were replaced by spec-zs (green dashed histogram). For the estimation of physical parameters, we restrict our sample to MIR-detected sgzKs with $1.4 \leq z \leq 2.5$, resulting in $N = 75$.

To build SEDs of sgzKs, we searched sgzK counterpart in FIR (*Herschel*) band. Among 75 MIR-detected sgzKs, 16 sgzKs have FIR detection. When there are multiple optical candidates including an sgzK within the beam size of FIR band, we also used LR analysis to find out how much the sgzK contributes to FIR band. If the reliability of sgzK is $R \geq 0.8$, we concluded that the sgzK is a robust contributor to the FIR band. On the other hand, we considered that the sgzK is a less robust contributor to the FIR band when the reliability of sgzK is $R < 0.8$. For these sgzKs, the photometric data in FIR bands are treated as upper limits of sgzKs. For the same reason, IR luminosity and SFR of these sgzKs are treated as upper limits, while AGN contribution of such sgzK is treated as a lower limit since its definition is $L_{\rm AGN}/L_{\rm IR}$.

SEDs of sgzKs were fitted by Code Investigating GALaxy Emission (CIGALE) v0.11 (Burgarella, Buat & Iglesias-Páramo 2005; Noll et al. 2009) to estimate physical parameters.[7] CIGALE enables us to estimate the physical parameters of sgzKs by comparing photometric data to modelled galaxy SEDs. It generates model SEDs based on emissions from stellar and AGN, and considers dust attenuation to estimate energy balance between dust absorption and its re-emission at longer wavelength bands. AGN templates of Fritz et al. (2006) are used to generate AGN emission. The contribution of AGN to the luminosity, fracAGN, is given as an input parameter. Because the

[7] http://cigale.lam.fr

Table 2. Model and the range of input parameters used for the SED fitting by CIGALE. The numbers in parentheses were applied to only two sgzK galaxies in order to improve fit result. Parameters that are not listed in this table adopted the default values presented in CIGALE.

Model and input parameter	Range
Star formation history: sfh2exp	
e-folding time of the main stellar population model (Myr)	1000, 3000, 5000
e-folding time of the late starburst population model (Myr)	30, 60, 100
Mass fraction of the late burst population	0.05, 0.1, 0.3, 0.5
Age of the main stellar population in the galaxy (Myr)	500, 1000, 3000, 5000
Age of the late burst (Myr)	(30), 100, 300, 500
Stellar population: m2005 (Maraston 2005)	
Initial mass function	Salpeter
Metallicity	0.02
Dust attenuation: dustatt calzleit (Calzetti et al. 2000)	
Colour excess for the young population	0.01, 0.1, 0.3, 0.5, 0.7, 0.9, 1.1, (1.7)
Dust emission: dl2014 (Draine & Li 2007)	
Mass fraction of PAH	0.47, 1.77, 3.9, 5.26, 6.63
Minimum radiation field	0.5, 1.0, 2.5, 5.0, 7.0, 10.0, 25.0, 40.0
Power-law index	1.0, 1.5, 2.0, 2.5, 3.0
AGN emission: fritz2006 (Fritz, Franceschini & Hatziminaoglou 2006)	
Ratio of the maximum to minimum radius of the torus	60.0
Optical depth at 9.7 μm	1.0, 6.0
Radial gas density gradient in the torus	−0.5
Angular gas density gradient in the torus	4.0
Full opening angle of the dust torus (°)	100.0
Angle between equatorial axis and line of sight (°)	10.1, 50.1, 80.1
AGN fraction	0–0.98 with the interval of 0.02

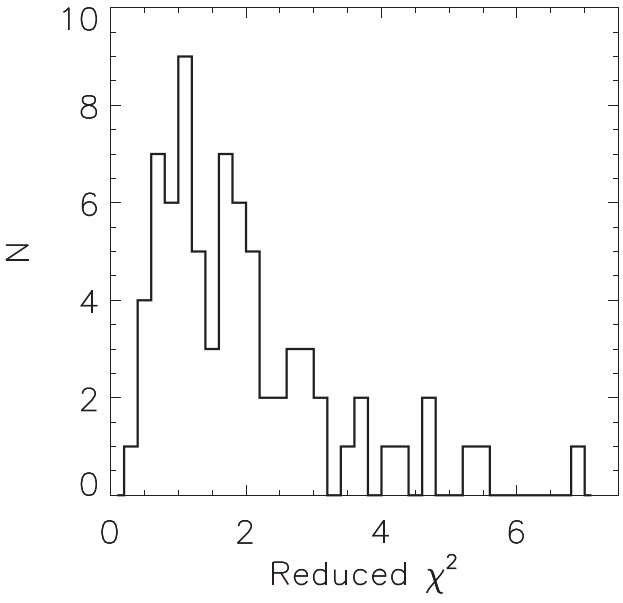

Figure 11. The result of SED fits using CIGALE for 75 MIR-detected sgzKs. The histogram shows a reduced χ^2 distribution obtained from CIGALE. 96 per cent of the samples have the reduced χ^2 lower than 5.

contribution of AGN in sgzK is one of the important results in this study, we consider a lot of values of fracAGN with equally spaced interval (ΔfracAGN = 0.02) from 0 to 0.98. Input parameters for stellar population, star formation history, dust emission, and dust attenuation are presented in Table 2. The quality of SED fits for 75 MIR-detected sgzKs is presented in Fig. 11, and some examples for the SED fit are presented in Fig. 12. We adopted 50 per cent completeness levels of 100 and 250 μm as constraints in the SED fit procedure. At first, for example, the SED fit was conducted based on only the observed photometric data. After that, if the best-fitting model exceeded 50 per cent completeness level in 100 or 250 μm such as black dotted lines in panels (c) and (d), the SEDs of such samples were fitted again by inserting 50 per cent completeness level of 100 or 250 μm as an upper limit in the corresponding band to obtain reasonable fit models. Thus, for the samples such as those in panels (c) and (d), SFR and IR luminosity are treated as upper limits. For the same reason, AGN contribution of such sample is treated as a lower limit.

4.3 Physical quantities

Physical quantities for 75 MIR-detected sgzKs are presented in Fig. 13. In terms of IR luminosity, most sgzKs are classified as luminous IR galaxies (LIRGs) or ULIRGs. Among them, most of the sgzKs with FIR detection correspond to ULIRGs. Stellar masses for sgzKs were estimated by fitting photometric data of CFHT bands to avoid the contributions from AGN and dust in MIR and FIR bands. As shown in panel (b), sgzKs have large stellar masses. Median and mean stellar masses are 9.5×10^{10} and 1.2×10^{11} $M_\odot$, respectively, which are similar to the results in the literature. Kong et al. (2006) reported $\sim 10^{11}$ $M_\odot$ as the median stellar mass of sBzKs with $K_{Vega} < 20$. Fang et al. (2012) reported that the median stellar mass of sgzKs with $K < 22$ is $\sim 8.8 \times 10^{10}$ $M_\odot$, and Daddi et al. (2004) reported typical stellar masses of $\sim 10^{11}$ $M_\odot$ for BzKs with $K_{Vega} < 20$. Median and mean SFRs are 162 and 205 $M_\odot$ yr^{-1}, respectively, which are comparable to the previous results. Fang et al. (2012) found 184 $M_\odot$ yr^{-1} as the median SFR of sgzKs with $K < 22$. Daddi et al. (2004) reported a typical SFR of $\sim$200 $M_\odot$ yr^{-1} for sBzKs with

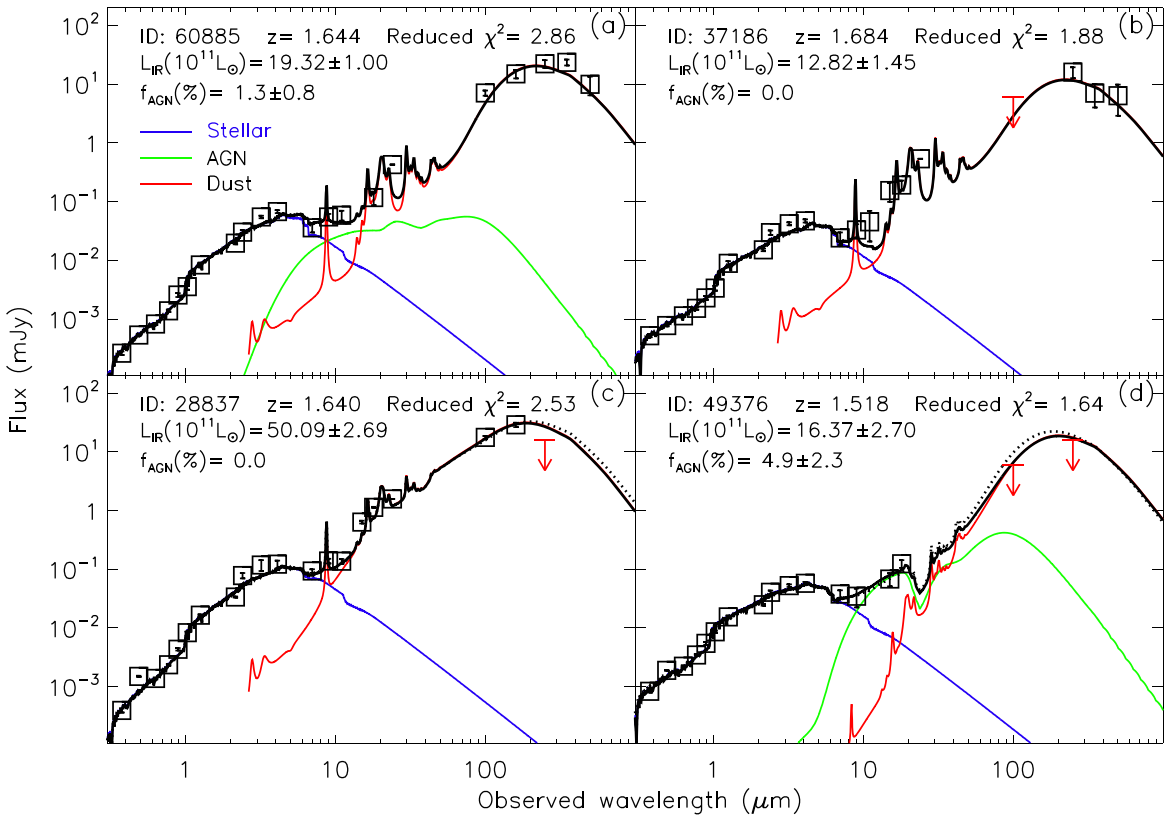

Figure 12. Examples for the SEDs of sgzKs and best-fitting models. Open squares show photometric data in CFHT, *AKARI*, and *Herschel* bands. Red arrows show 50 per cent completeness levels in 100 and 250 μm. Black solid lines show the best-fitting models consisting of three components such as stellar (blue), AGN (green), and dust (red). AGN luminosity (L_{AGN}) and IR luminosity are estimated by integrating the green and black solid lines, respectively, in the rest-frame wavelength 8–1000 μm. The contribution of AGN, f_{AGN}, is estimated by the ratio of AGN luminosity to the IR luminosity. 50 per cent completeness levels in 100 and 250 μm were given as upper limits in the SED fit procedure. In panel (b), the best-fitting model does not exceed 50 per cent completeness level at 100 μm, where the object is not detected. On the other hand, in panels (c) and (d), the best-fitting models (black dotted lines) exceed 50 per cent completeness level in 100 or 250 μm. In that case, the SEDs were fitted again by inserting 50 per cent completeness level of 100 or 250 μm as an upper limit to obtain reasonable fit models (black solid lines). The ID of the sample comes from the CFHT catalogue (Oi et al. 2014).

$K_{Vega} < 20$, and Kong et al. (2006) also reported ∼190 $M_\odot$ yr^{-1} as the median SFR of sBzKs with $K_{Vega} < 20$. In panels (b) and (c), data points denoted by the square are fitted by the Bayesian linear regression routine (Kelly 2007)[8] that considers uncertainties in both log (s)SFR and log M_*. Black solid lines are the fitted functions parameterized as

$$\log(\text{s})\text{SFR} = \alpha + \beta(\log M_* - 11.0), \quad (25)$$

where the best-fitting value and uncertainty for the normalization α and slope β are determined by the median and 1σ confidence interval of the probability distribution function. Dashed lines in panel (b) show the main sequence for star-forming galaxies at $1.5 < z < 2.0$ (blue) and $2.0 < z < 2.5$ (red), respectively (Whitaker et al. 2014). They show positive correlation between SFR and stellar mass, and show larger SFR at higher redshift at a fixed stellar mass. Considering the redshift range of our data ($1.4 \leq z \leq 2.5$), our result (black solid line) in panel (b) is comparable with the result for star-forming galaxies in the literature (dashed lines). In panel (c), as shown, sSFR and stellar mass are anticorrelated, representing that star formation is efficient more in low-mass sgzKs than in high-mass sgzKs. In panels (b) and (c), sgzKs with FIR detection show more SFR activity compared to those without FIR detection. Although, previous studies reported that sSFR of sgzKs increases with increasing redshift at a fixed stellar mass, representing more SFR activity at higher redshift (Dunne et al. 2009; Fang et al. 2012), such feature is unclear in this study due to the small number of samples.

As shown in Fig. 7, the correlation length of sgzKs is comparable to those of massive galaxies such as ULIRGS at comparable redshift, EROs, DOGs, and SMGs with z = 2–3, which implies possible evolutionary connections among them. Thus, sgzKs could be a certain stage in the evolution of massive galaxies. In the scenario for massive galaxy evolution, galaxies would pass both the star formation-dominated phase and the AGN-dominated phase. Therefore, in order to understand the evolution of sgzKs, the estimation of AGN activity in sgzKs is useful. X-ray observation data were usually used to find out the number ratio of AGNs in sgzK galaxies. Daddi et al. (2005) reported that ∼22 per cent of sBzKs with $K_{Vega} < 20$ are likely an AGN-dominated phase due to the detection in the hard X-ray band, and Kong et al. (2006) reported that ∼25 per cent of sBzKs can be classified as AGNs by the X-ray data. However, such methods are able to detect only AGN-dominant sgzKs, and the results depend on

[8]IDL code LINMIX_ERR.PRO is available at https://idlastro.gsfc.nasa.gov/.

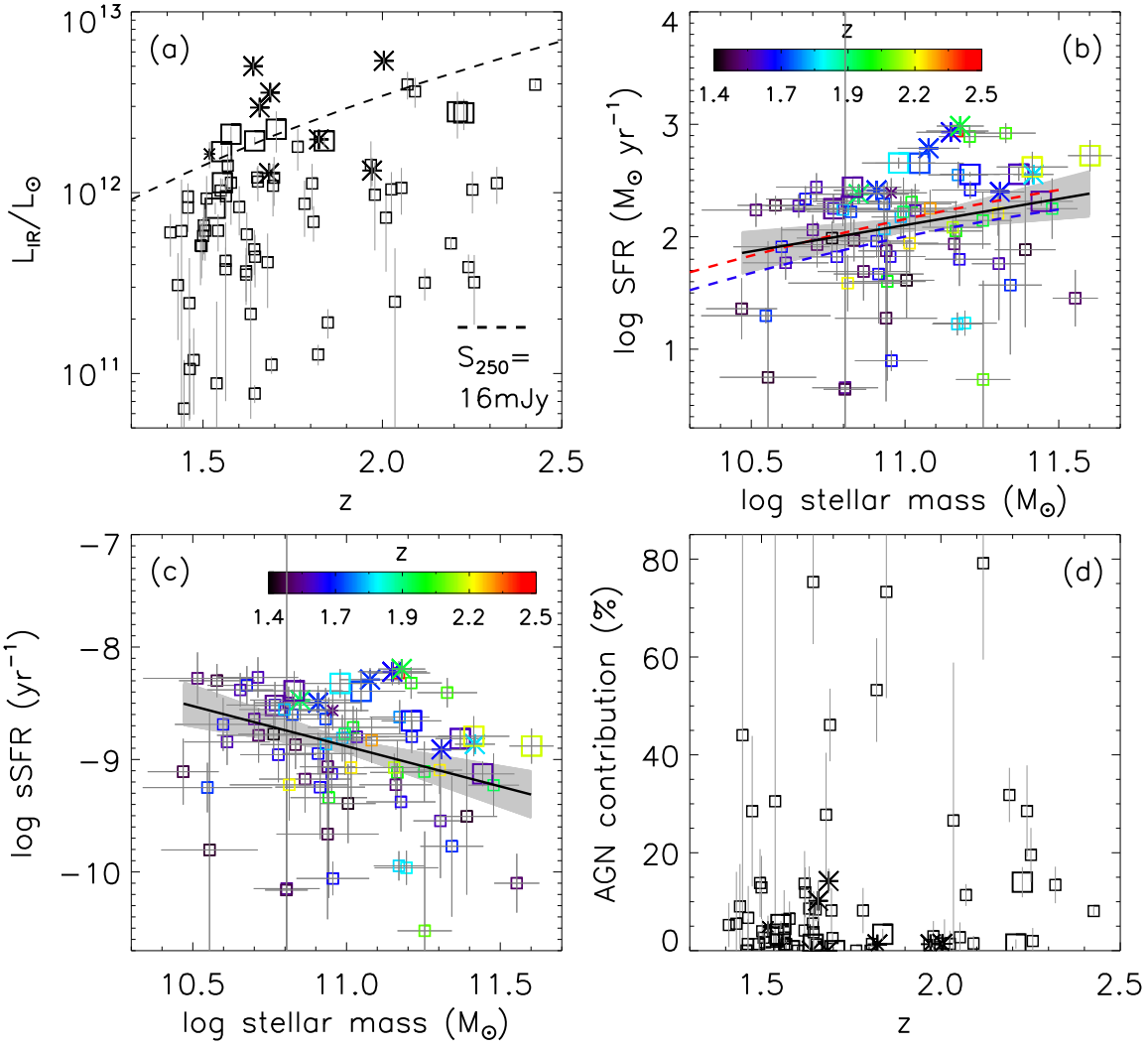

Figure 13. Physical parameters for 75 MIR-detected sgzKs with $K_s < 21.5$ (median $z = 1.645$). Large symbols represent sgzKs with FIR (*Herschel*) detection. Data points denoted by the asterisk in panels (a), (b), and (c) represent upper limits, while those in panel (d) represent lower limits (see section 4.2 for details). In panels (b) and (c), solid lines are the fitted lines for our data. The grey shaded regions show 1σ uncertainties in the normalization and slope. The fitting was conducted using only the data points denoted by the square. (a) IR luminosity as a function of redshift. The luminosity limit of 250 μm (dashed line) is calculated by the combination of a single temperature modified blackbody (MBB) function, $S_\nu = \nu^\beta B_\nu(T)$, and a power-law SED, $S_\nu = \nu^{-\alpha}$, for the Wien side of the MBB function. $B_\nu(T)$ is the Planck function. β is dust emissivity index, α is MIR power-law slope, and T represents dust temperature, which are assumed to be $\beta = 1.5$, $\alpha = 2$, and $T = 20$ K, respectively. Flux density of 16 mJy is the 50 per cent completeness level in 250 μm. (b) SFR as a function of stellar mass. For the fitted line, the corresponding values for α and β in equation (25) are 2.10 ± 0.06 and 0.47 ± 0.26, respectively. Dashed lines represent polynomial fits for star-forming galaxies at $1.5 < z < 2.0$ (blue) and $2.0 < z < 2.5$ (red), respectively (Whitaker et al. 2014). (c) sSFR as a function of stellar mass. For the fitted line, the corresponding values for α and β in equation (25) are -8.88 ± 0.06 and -0.71 ± 0.25, respectively. (d) AGN contribution as a function of redshift. The AGN contribution is estimated by the ratio of AGN luminosity to the IR luminosity in the rest-frame wavelength 8–1000 μm.

the sensitivity of X-ray data. On the other hand, it is known that MIR SED fit is an effective method for the selection of AGN candidates. Fang et al. (2012) investigated the number fraction of AGNs in gzK galaxies using *Spitzer*/IRAC-colour criteria and the slope of SED at MIR bands. They reported that ∼10 per cent of IRAC-bands-detected gzKs can be classified as AGNs. Krumpe et al. (2015) estimated the contribution of AGN in IR-selected sources by MIR SED fits, and found that the AGN contribution determined by the MIR SED fits has a positive correlation with the X-ray detection rate. With the help of continuous IR coverage by nine photometric bands from 2.4 to 24 μm, we investigated the ratio of AGN luminosity to the IR luminosity in each sgzK galaxy by the SED fit method. As shown in Fig. 13(d), MIR-detected sgzKs have a variety of AGN contributions ranging from 0 to 80 per cent. Considering the data points denoted by the square in Fig. 13(d), the number ratio of sgzKs with larger AGN contribution than 10 per cent is 30 per cent.

As an additional indicator of AGN activity in sgzKs, we estimated Eddington ratio ($\lambda_{Edd} = L_{AGN,bol}/L_{Edd}$, where the Eddington luminosity L_{Edd} is $1.26 \times 10^{38} M_{BH}/M_\odot$ erg s^{-1}) for 75 MIR-detected sgzKs. AGN bolometric luminosity $L_{AGN,bol}$ is given by CIGALE. For the estimation of black hole mass M_{BH}, we used the scaling relation between black hole mass M_{BH} and host galaxy stellar mass

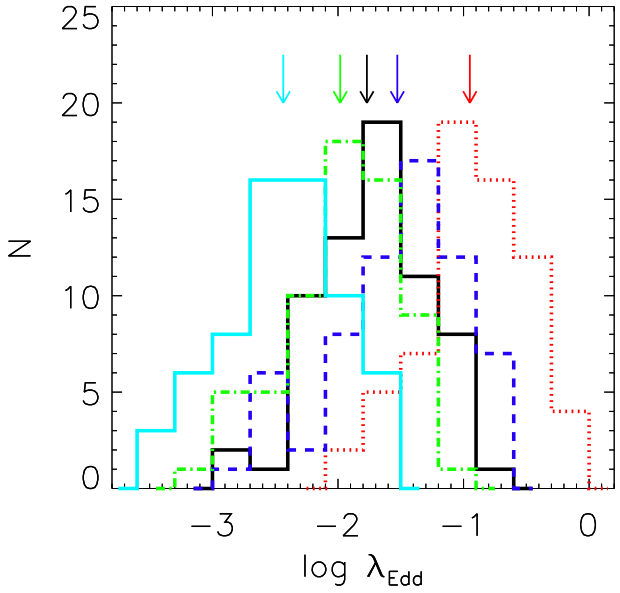

Figure 14. Eddington ratio distributions for 75 MIR-detected sgzKs. Histograms show the results based on the M_{BH}–M_* relations in the literature: Reines & Volonteri (2015, red, sky blue), Bentz & Manne-Nicholas (2018, blue, green), and Ding et al. (2020, black). The arrow shows the median for each histogram. For convenience, sgzKs with $L_{AGN,bol} = 0$ are not presented, while they are included in the estimation of the median of Eddington ratio distribution. The results are summarized in Table 3.

Table 3. Eddington ratios for 75 MIR-detected sgzKs. Column 1: reference for the M_{BH}–M_* relation. Column 2: the median of Eddington ratio distribution. Column 3: the number ratio of sgzKs with $\lambda_{Edd} > 0.1$.

Reference	Median λ_{Edd}	$f(\lambda_{Edd} > 0.1)$
Reines & Volonteri (2015)[a]	0.112	52.0 per cent
Reines & Volonteri (2015)[b]	0.004	0.0 per cent
Bentz & Manne-Nicholas (2018)[c]	0.030	10.7 per cent
Bentz & Manne-Nicholas (2018)[d]	0.010	0.0 per cent
Ding et al. (2020)	0.017	4.0 per cent

[a] The M_{BH}–M_* relation derived from broad-line AGNs.
[b] The M_{BH}–M_* relation derived from elliptical galaxies and spiral/S0 galaxies with classical bulges in Kormendy & Ho (2013).
[c, d] The M_{BH}–M_* relations come from equations (14) and (15), respectively, in Bentz & Manne-Nicholas (2018), where the two equations are derived by different methods in the stellar mass calculation.

M_* (i.e. the M_{BH}–M_* relation)[9] in the literature rather than the broad-line width because sgzKs in this study are not broad-line-selected samples. However, the M_{BH}–M_* relations in the literature are not identical partly due to sample selection effects or the difference in the stellar mass calculation method. We adopted several M_{BH}–M_* relations in the literature to estimate black hole mass, and found that they give a variety of black hole masses for a given sgzK stellar mass, resulting in a wide range of Eddington ratios for sgzKs. As shown in Fig. 14 and Table 3, the number ratio of sgzKs with $\lambda_{Edd} > 0.1$ ranges from 0 to 52 per cent. The median of Eddington ratio distribution for sgzKs ranges from 0.004 to 0.112. According to the studies for optical-, IR-, or X-ray-selected broad-line AGNs, a median (or peak) of Eddington ratio distribution for AGNs is around 0.1 (Kollmeier et al. 2006; Trump et al. 2009; Merloni et al. 2010; Suh et al. 2015, 2020). Although, on average, Eddington ratio of sgzks seems to be smaller than that of broad-line AGNs in the literature, the difference is not clear due to a wide range of Eddington ratios in sgzKs. Therefore, in order to adopt Eddington ratio as an indicator of AGN activity in sgzKs, further studies with broad-line-selected samples are needed for the estimation of reliable black hole mass.

[9]We used the local M_{BH}–M_* relation under the assumption that there is no significant evolution over redshift in the M_{BH}–M_* relation as presented in the literature (e.g. Sun et al. 2015; Suh et al. 2020).

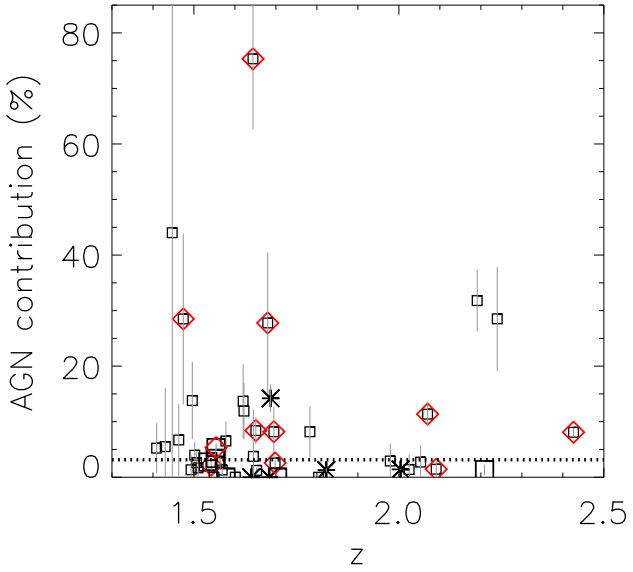

Figure 15. AGN contribution as a function of redshift for 46 MIR-detected sgzKs that are located within the X-ray survey area. 11 MIR-detected sgzKs with X-ray detection are denoted by the red diamond. The dotted line shows the median AGN contribution of 46 MIR-detected sgzKs. Other symbols are the same as those in Fig. 13(d).

As shown in Fig. 1, part of the NEP-Deep Field was surveyed by *Chandra* observations that detect sources down to 10^{-15} erg s^{-1} cm^{-2} in the 0.5–7 keV band (Krumpe et al. 2015). 240 out of 428 sgzKs with $K_s < 21.5$ are located within the X-ray survey area (i.e. the area within the red box in Fig. 1). Among them, 32 sgzKs (i.e. 13 per cent) are cross-matched with the X-ray sources. Fig. 15 focuses only on MIR-detected sgzKs that are located within the X-ray survey area. 46 out of 75 MIR-detected sgzKs are located within the X-ray survey area. Among them, 11 MIR-detected sgzKs (i.e. 24 per cent) are cross-matched with the X-ray sources (red diamonds in Fig. 15). If we divide 46 MIR-detected sgzKs into 2 groups based on the dotted line (i.e. the median AGN contribution of 46 MIR-detected sgzKs) in Fig. 15, X-ray detection rates for the groups above and below the dotted line are 35 and 13 per cent, respectively. The group with relatively large AGN contribution shows more X-ray detection rate than the other group. Although the number of sample is small, Fig. 15 shows that the AGN contribution estimated by the SED fit seems to be an effective indicator for selecting AGN candidates as suggested in Krumpe et al. (2015).

5 SUMMARY

We studied the clustering property and physical parameters of sgzKs based on the photometric data from the CFHT/MegaCam

and CFHT/WIRCam surveys in the *AKARI* NEP-Deep Field. *gzK*-colour selection criteria were used to select galaxies at $z > 1.4$. We estimated two-point correlation functions for two magnitude-limited sgzKs: $K_s < 21.1$ ($N = 234$) and $K_s < 21.5$ ($N = 428$). The two-point correlation function was fitted using a single power-law function, $\omega(\theta) = A_\omega \theta^{-\delta}$, with the fixed δ of 0.8. Based on the fitted function, the correlation length and bias of sgzKs were estimated. The evolution of bias for dark matter haloes hosting sgzKs was estimated in order to study the evolution of sgzKs. Physical parameters and AGN contribution were estimated for 75 MIR-detected sgzKs with $K_s < 21.5$. The study is summarized as follows:

(i) Two-point correlation functions for two magnitude-limited sgzKs are comparable to the previous results. In addition to the results in the literature, our result shows K_s magnitude dependence of the clustering strength, i.e. decreasing clustering strength with increasing K_s-band magnitude. The correlation lengths of sgzKs with $K_s < 21.1$ and 21.5 are 13.98 ± 2.88 and 9.13 ± 1.69 h^{-1} Mpc, respectively. The bias factors of sgzKs with $K_s < 21.1$ and 21.5 are 5.79 ± 1.07 and 4.00 ± 0.67, respectively, representing that sgzKs with $z \sim 1.7$ reside in dark matter haloes more massive than 10^{13} $M_\odot$.

(ii) To investigate the evolutionary link between sgzKs and local galaxies, we estimated the bias evolution for dark matter haloes hosting sgzKs. We found that haloes that host sgzKs with $K_s < 21.5$ at $z \sim 1.7$ evolve into haloes hosting local massive galaxies with $\sim$6 L^*. This suggests that sgzKs with $K_s < 21.5$ are likely possible predecessors of local massive galaxies.

(iii) The bias factor of sgzKs with $K_s < 21.5$ at $z \sim 1.7$ is similar to that of pEROs with $K_s < 20.9$ at $z \sim 1.2$. In addition, the evolutionary track of bias factor for host haloes of sgzKs with $K_s < 21.5$ is similar to that of pEROs with $K_s < 20.9$, implying a possible evolutionary link between the two galaxy populations.

(iv) Physical parameters were estimated by fitting SEDs of 75 MIR-detected sgzKs with $K_s < 21.5$. In terms of IR luminosity, most sgzKs are classified as LIRGs or ULIRGs. The median values of stellar mass and SFR are 9.5×10^{10} $M_\odot$ and 162 $M_\odot$ yr^{-1}, respectively. Stellar mass and sSFR are anticorrelated, which represents that star formation is efficient more in low-mass sgzKs than in high-mass sgzKs.

(v) For 75 MIR-detected sgzKs, AGN contribution, the ratio of AGN luminosity to the IR luminosity in the rest-frame wavelength 8–1000 μm, was estimated. MIR-detected sgzKs have a variety of AGN contributions ranging from 0 to 80 per cent. The number ratio of sgzKs with larger AGN contribution than 10 per cent is 30 per cent. MIR-detected sgzKs with large AGN contribution show more X-ray detection rates.

The upcoming new photometric data sets from Subaru/Hyper Suprime-Camera surveys with *grizy* bands over $\sim$5.4 deg^2 (Goto et al. 2017) and CFHT K_s-band observations will provide larger number of gzK galaxies in the NEP field, which enables us to investigate gzK galaxies more precisely. For example, the redshift dependence of sSFR discussed in Fig. 13(c) and the evolutionary connection between sgzKs and pEROs can be further clarified by larger number of gzK galaxies. Moreover, we can investigate the correlation between clustering property and physical parameters, which will provide information about an environmental effect on the physical parameters of gzKs.

ACKNOWLEDGEMENTS

We thank the referee for the careful reading and constructive comments to improve this draft. W-SJ acknowledges support from the National Research Foundation of Korea (NRF) grant funded by the Ministry of Science and ICT (MSIT) of Korea (NRF-2018M1A3A3A02065645). HShim acknowledges the support from the National Research Foundation of Korea (NRF) grant number 2018R1C1B6008498, funded by Korea government (MSIT). MK was supported by the National Research Foundation of Korea (NRF) grant funded by the Korea government (MSIT) (number 2020R1A2C4001753). TG acknowledges the support by the Ministry of Science and Technology of Taiwan through grant 105-2112-M-007-003-MY3. TM is supported by UNAM-DGAPA (PASPA and PAPIIT IN111319) and CONACyT 252531.

DATA AVAILABILITY

The data generated in this study (e.g. photo-z and the result of SED fits for 75 MIR-detected sgzK galaxies) will be shared on reasonable request to the corresponding author.

REFERENCES

Aird J., Coil A. L., Georgakakis A., Nandra K., Barro G., Pérez-González P. G., 2015, MNRAS, 451, 1892
Arcila-Osejo L., Sawicki M., 2013, MNRAS, 435, 845
Arnouts S., Cristiani S., Moscardini L., Matarrese S., Lucchin F., Fontana A., Giallongo E., 1999, MNRAS, 310, 540
Bentz M. C., Manne-Nicholas E., 2018, ApJ, 864, 146
Bielby R. et al., 2012, A&A, 545, A23
Blanc G. A. et al., 2008, ApJ, 681, 1099
Brodwin M. et al., 2008, ApJ, 687, L65
Burgarella D., Buat V., Iglesias-Páramo J., 2005, MNRAS, 360, 1413
Bussmann R. S. et al., 2009, ApJ, 705, 184
Bussmann R. S. et al., 2012, ApJ, 744, 150
Calzetti D., Armus L., Bohlin R. C., Kinney A. L., Koornneef J., Storchi-Bergmann T., 2000, ApJ, 533, 682
Daddi E., Cimatti A., Renzini A., Fontana A., Mignoli M., Pozzetti L., Tozzi P., Zamorani G., 2004, ApJ, 617, 746
Daddi E. et al., 2005, ApJ, 631, L13
Dey A., The NDWFS/MIPS Collaboration, 2009, in Weimin W., Zhaoqing Y., Zhijian L., Zhu C., eds, ASP Conf. Ser. Vol. 408, The Starburst-AGN Connection. Astron. Soc. Pac., San Francisco, p. 411
Dey A. et al., 2008, ApJ, 677, 943
Ding X. et al., 2020, ApJ, 888, 37
Draine B. T., Li A., 2007, ApJ, 657, 810
Dunne L. et al., 2009, MNRAS, 394, 3
Elston R., Rieke G. H., Rieke M. J., 1988, ApJ, 331, L77
Fakhouri O., Ma C.-P., Boylan-Kolchin M., 2010, MNRAS, 406, 2267
Fang G., Kong X., Chen Y., Lin X., 2012, ApJ, 751, 109
Farrah D. et al., 2006, ApJ, 643, L139
Fritz J., Franceschini A., Hatziminaoglou E., 2006, MNRAS, 366, 767
Goto T. et al., 2015, MNRAS, 452, 1684
Goto T. et al., 2017, Publ. Korean Astron. Soc., 32, 225
Groth E. J., Peebles P. J. E., 1977, ApJ, 217, 385
Gruppioni C. et al., 2013, MNRAS, 432, 23
Hartley W. G. et al., 2008, MNRAS, 391, 1301
Hayashi M., Shimasaku K., Motohara K., Yoshida M., Okamura S., Kashikawa N., 2007, ApJ, 660, 72
Hickox R. C. et al., 2012, MNRAS, 421, 284
Ilbert O. et al., 2006, A&A, 457, 841
Ilbert O. et al., 2009, ApJ, 690, 1236
Imai K., Pearson C. P., Matsuhara H., Wada T., Oyabu S., Takagi T., Fujishiro N., Hanami H., 2008, ApJ, 683, 45

Ishikawa S., Kashikawa N., Toshikawa J., Onoue M., 2015, MNRAS, 454, 205
Jeon Y., Im M., Kang E., Lee H. M., Matsuhara H., 2014, ApJS, 214, 20
Kelly B. C., 2007, ApJ, 665, 1489
Kim J.-W., Edge A. C., Wake D. A., Stott J. P., 2011, MNRAS, 410, 241
Kim J.-W. et al., 2014, MNRAS, 438, 825
Kollmeier J. A. et al., 2006, ApJ, 648, 128
Kong X. et al., 2006, ApJ, 638, 72
Kormendy J., Ho L. C., 2013, ARA&A, 51, 511
Krumpe M. et al., 2015, MNRAS, 446, 911
Landy S. D., Szalay A. S., 1993, ApJ, 412, 64
Limber D. N., 1953, ApJ, 117, 134
Madau P., Dickinson M., 2014, ARA&A, 52, 415
Magliocchetti M., Lapi A., Negrello M., De Zotti G., Danese L., 2014, MNRAS, 437, 2263
Magnelli B. et al., 2013, A&A, 553, A132
Mancini C., Renzini A., Daddi E., Rodighiero G., Berta S., Grogin N., Kocevski D., Koekemoer A., 2015, MNRAS, 450, 763
Maraston C., 2005, MNRAS, 362, 799
Markwardt C. B., 2009, in David A. B., Daniel D., Patrick D., eds, ASP Conf. Ser. Vol. 411, Astronomical Data Analysis Software and Systems XVIII. Astron. Soc. Pac., San Francisco, p. 251
Matsuhara H. et al., 2006, PASJ, 58, 673
McCracken H. J. et al., 2010, ApJ, 708, 202
Merloni A. et al., 2010, ApJ, 708, 137
Mo H. J., White S. D. M., 2002, MNRAS, 336, 112
Murata K. et al., 2013, A&A, 559, A132
Narayanan D. et al., 2010, MNRAS, 407, 1701
Nayyeri H. et al., 2018, ApJS, 234, 38
Nikoloudakis N., Shanks T., Sawangwit U., 2013, MNRAS, 429, 2032
Noll S., Burgarella D., Giovannoli E., Buat V., Marcillac D., Muñoz-Mateos J. C., 2009, A&A, 507, 1793
Ohyama Y. et al., 2018, A&A, 618, A101
Oi N. et al., 2014, A&A, 566, 60
Palamara D. P. et al., 2013, ApJ, 764, 31
Pearson C. et al., 2017, Publ. Korean Astron. Soc., 32, 219
Pearson C. et al., 2019, PASJ, 71, 13
Peebles P. J. E., 1980, The Large-Scale Structure of the Universe. Princeton Univ. Press, Princeton, NJ
Planck Collaboration XVI, 2014, A&A, 571, A16
Prevot M. L., Lequeux J., Maurice E., Prevot L., Rocca-Volmerange B., 1984, A&A, 132, 389
Reines A. E., Volonteri M., 2015, ApJ, 813, 82
Roche N., Eales S. A., Hippelein H., Willott C. J., 1999, MNRAS, 306, 538
Salvato M. et al., 2009, ApJ, 690, 1250
Seo H. et al., 2018, J. Korean Astron. Soc., 51, 49
Seo H. et al., 2019, PASJ, 71, 96
Sheth R. K., Mo H. J., Tormen G., 2001, MNRAS, 323, 1
Shim H. et al., 2013, ApJS, 207, 37
Shin J., Shim H., Hwang H. S., Ko J., Lee J. C., Utsumi Y., Hwang N., Park B.-G., 2017, J. Korean Astron. Soc., 50, 61
Silverman J. D. et al., 2008, ApJ, 679, 118
Suh H., Civano F., Trakhtenbrot B., Shankar F., Hasinger G., Sanders D. B., Allevato V., 2020, ApJ, 889, 32
Suh H., Hasinger G., Steinhardt C., Silverman J. D., Schramm M., 2015, ApJ, 815, 129
Sun M. et al., 2015, ApJ, 802, 14
Sutherland W., Saunders W., 1992, MNRAS, 259, 413
Takagi T. et al., 2012, A&A, 537, A24
Toba Y. et al., 2017, ApJ, 835, 36
Trump J. R. et al., 2009, ApJ, 700, 49
Whitaker K. E. et al., 2011, ApJ, 735, 86
Whitaker K. E. et al., 2014, ApJ, 795, 104
Wilkinson A. et al., 2017, MNRAS, 464, 1380
Zehavi I. et al., 2011, ApJ, 736, 59

This paper has been typeset from a TEX/LATEX file prepared by the author.